International Information and Engineering Technology Association
Advancing the World of Information and Engineering

Journal Européen des Systèmes Automatisés
Vol. 58, No. 3, March, 2025, pp. 421-434
Journal homepage: http://iieta.org/journals/jesa

Sensorless Wind Speed Estimation Using PSO for Multi-Objective Finite-State Predictive Torque Control in Grid-Connected Wind Turbines

Marouane Ahmed Ghodbane[1*], Toufik Mohamed Benchouia[1], Mohamed Chebaani[1], Mohamed Becherif[2], Amar Gloea[1], Abdelmoumen Ghilani[3], Zakaria Alili[4]

[1] LGEB laboratory, University of Biskra, Biskra 07000, Algeria
[2] FClab FR CNRS, University of Bourgogne Franche-Comté/UTBM, Belfort 90010, France
[3] LMSE laboratory, University of Biskra, Biskra 07000, Algeria
[4] LEE laboratory, University of Msila, Msila 28000, Algeria

Corresponding Author Email: marouane.ghodbane@univ-biskra.dz

https://doi.org/10.18280/jesa.580302

Received: 7 February 2025
Revised: 11 March 2025
Accepted: 21 March 2025
Available online: 31 March 2025

Keywords:
wind energy, PMSG, PSO, sensorless, finite state, predictive torque, weighting factor

ABSTRACT

This paper introduces a novel approach to improving the performance of grid-connected wind turbines by combining Particle Swarm Optimization (PSO)-based sensorless wind speed estimation with Multi-Objective Finite State Predictive Torque Control (FSPTC). Accurate wind speed estimation is crucial for efficient turbine operation, especially in sensorless systems where traditional sensors may be expensive or unreliable. The proposed method uses PSO to estimate wind speed. In traditional FS-PTC, fine-tuning these factors is necessary to balance torque and flux dynamics, which can complicate the control process and reduce efficiency. Our new method simplifies things by using a multi-objective finite-state predictive control strategy that simultaneously optimizes torque and flux without relying on these weighting factors, by substituting the singular cost function with two distinct cost functions. Thus, simplifying the control architecture. To evaluate our approach, we performed extensive MATLAB simulations and experimental validation with real-time control implemented through ControlDesk, dSPACE DS1104 and the DSP LAUNCHXL-F28379D under various wind conditions. The results were promising, showing significant improvements in how quickly the system stabilizes torque and flux outputs. Furthermore, our method reduces the computational load compared to conventional approaches, making it more practical for real-time applications in wind energy systems.

1. INTRODUCTION

The demand for renewable energy sources has increased due to environmental issues and the necessity for sustainable power generation. Wind energy has emerged as a significant alternative [1], due to its beneficial environmental effects and economic efficiency compared to traditional energy sources [2]. Permanent Magnet Synchronous Generators (PMSGs) are esteemed for their efficiency, reliability, and diminished maintenance needs within the diverse designs of variable speed wind turbine systems (VS-WTS), particularly in direct-drive wind turbine systems. PMSGs, Furthermore, it possesses superior inertia relative to other wind turbines [3, 4] in contrast to doubly-fed induction generators (DFIGs), obviate the necessity for a gearbox [5] thus enhancing overall system reliability and diminishing mechanical losses. Managing PMSG-based wind turbines poses difficulties owing to the inherently unpredictable characteristics of wind and the necessity to enhance energy conversion efficiency [6]. Conventional control techniques, including vector control and direct torque control (DTC), are frequently employed for PMSGs [7]. DTC, recognised for its rapid transient reaction and resilience to parameter fluctuations, is proficient in regulating the generator's torque and flux. Nonetheless, traditional DTC has significant torque ripples [8] and necessitates elevated sampling rates, leading to heightened computing requirements. Model Predictive Control (MPC) has emerged as a robust alternative for addressing these challenges, owing to its capacity to manage multivariable limitations and deliver rapid dynamic responses [9, 10].

Predictive Torque Control (PTC) and Predictive Flux Control (PFC), both variants of finite-control-set Model Predictive Control (FCS-MPC), are being progressively employed for the regulation of torque and flux in PMSGs [11]. A comprehensive analysis of predictive control schemes for power electronics is conducted in reference [12]. The fundamental principle is that a discrete model is employed to forecast the system's behaviour for each permissible sequence of control sets up to the prediction horizon. The control set that minimises a specified cost function is ultimately chosen for implementation in the subsequent sampling interval [9].

Nonetheless, these methods conventionally depend on weighting elements in the cost functions and has a direct influence on control performance to equilibrate control objectives including torque and flux [13]. Tuning weighting factors is frequently intricate due to the absence of a theoretical design methodology, typically depending on a trial-and-error technique that can be both time-consuming and inconsistent in dynamic settings [14]. Recent research suggest replacing weighting variables in predictive control with other strategies, such as reactive torque control and deadbeat principles [15], another suggested solution discussed in reference [16], a fuzzy-based PTC is implemented for the IM drive to mitigate the tweaking of weighting variables. However, adjustment of the priority coefficients assigned to the membership function is necessary. The multi-decision criteria-based TOPSIS and VIKOR approaches for IM drive control are provided in these studies [17, 18]. Nevertheless, in this process, weighting factor coefficients are not entirely eradicated. In another hand the wind speed at the blade level is measured by the anemometer. Nevertheless, the average wind speed acting across all blades may not be accurately captured by a single anemometer, as it only captures a localised measurement [19]. In this context wind PSO algorithm was integrated to estimate wind speed by optimizing the parameters of turbine model using turbine measurements like power output and generator speed. This helps minimize estimation errors and provides real-time, accurate wind speed data. These estimates were used to improve turbine control, including speed regulation and efficiency, all without relying on costly sensors.

This study concentrates on the simulation of Predictive Torque and Flux Control (PTFC) for PMSG based wind turbines in MATLAB Simulink and experimental validation with real-time control implemented through ControlDesk, dSPACE DS1104 and the DSP LAUNCHXL-F28379D, excluding the application of weighting factors and the anemometer. The main concept is the autonomous allocation of two distinct cost functions for the converter voltage vectors, succeeded by the assessment of the ranking of each prospective solution through an innovative method that eliminates the necessity for computationally demanding calculations, augment dynamic response, and bolster control resilience in the face of parameter changes.

2. SYSTEM MODELING

In directly driven VS-WTS, the PMSG is mechanically linked to the wind turbine. The stator windings are linked to the grid by a back-to-back voltage source converter (VSC) interconnected through a DC link bus and a filter as shown in Figure 1.

2.1 PMSG model

In directly driven VS-WTS, the PMSG is mechanically linked to the wind turbine. The stator windings are linked to the grid by a back-to-back VSC interconnected through a DC link bus and a filter.

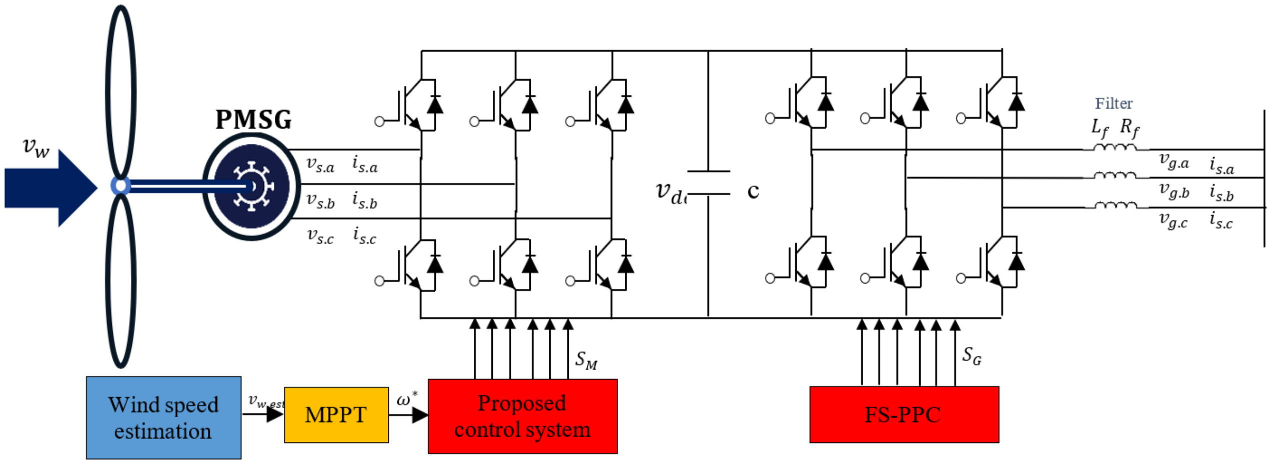

Figure 1. Configuration of a grid connected direct-drive PMSG WECS

The employed surface-mounted PMSG is distinguished by its subtle poles and a sinusoidal EMF pattern. The overall electrical and mechanical characteristics of the PMSG are integrated into the d-q reference frame using the Park transformation as follow [20]:

$$\left.\begin{aligned} v_{ds} &= R_s i_{ds} + \frac{d\psi_{ds}}{dt} - \omega_e \psi_{qs} \\ v_{qs} &= R_s i_{qs} + \frac{d\psi_{qs}}{dt} + \omega_e \psi_{ds} \end{aligned}\right\} \quad (1)$$

$$\left.\begin{aligned} \psi_{ds} &= L_d i_{ds} + \psi_{pm} \\ \psi_{qs} &= L_q i_{qs} \end{aligned}\right\} \quad (2)$$

R_s represents the stator resistance, ψ_{pm} represents the flux linkage, the variables L_d and L_q represent the inductances of the stator (armature) in d-q farm and ω_e is the electrical angular velocity, PMSG generates electromagnetic torque T_e defined by:

$$T_e = \frac{3p}{2}(\psi_{pm}.I_{qs}) \quad (3)$$

The mechanical equation of the PMSG is expressed as follows:

$$T_m = T_e + f\omega_r + J\frac{d\omega_r}{dt} \quad (4)$$

where, f is the friction coefficient, J is the total moment of inertia and T_m is the mechanical torque.

2.2 Wind turbine aerodynamic model

When wind interacts with the turbine, it produces mechanical power that propels the generator's rotor. The generator's power output is diminished owing to the turbine's inertia and frictional forces. The mechanical power output and torque of a Horizontal Axis Wind Turbine (HAWT) are as follows [21]:

$$P_m = \frac{1}{2} C_p(\lambda, \beta).\rho.\pi.R^2.v^3 \tag{5}$$

$$T_m = \frac{P_m}{\Omega_m} = \frac{1}{2} \frac{C_p(\lambda, \beta).\rho.\pi.R^2.v^3}{\Omega_m} \tag{6}$$

where, the C_p represents how effectively the turbine transforms the wind's kinetic energy into mechanical energy and can be caluted by the formula:

$$C_p(\lambda, \beta) = C_1 \left(\frac{C_2}{\lambda_i} - C_3 \beta - C_4 \right) e^{\frac{-C_5}{\lambda_i}} + C_6 \lambda \tag{7}$$

$$\frac{1}{\lambda_i} = \frac{1}{\lambda + 0.08\beta} - \frac{0.035}{1 + \beta^3} \tag{8}$$

with, λ is tip-speed ratio refers to the ratio of the tip of a rotating blade to the speed of the wind and can calculated as shown in Eq. (9), Ω_m is the mechanical angular speed of the turbine (in rad/s), R is the radius of the turbine blade and C_{1-6} Are the turbine coefficients, the approximated coefficient values are given as [22]:

$C_1 = 0.5167$, $C_3 = 116$, $C_3 = 0.4$
$C_4 = 5$, $C_5 = 21$, and $C_6 = 0.0068$

From TSR- C_p characteristics shown in Figure 2 The optimal C_p value denoted by $C_{p.opt}$ is typically around 0.48 when the λ this means the turbine reaches its maximum efficiency, extracting the most power possible from the wind, when it operates at this specific value $C_{p.opt}$ [23]:

$$\lambda = R \frac{\Omega_t}{v} \tag{9}$$

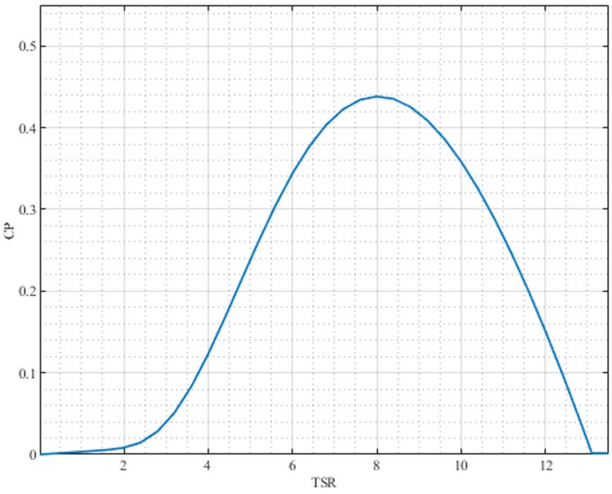

Figure 2. Real TSR - C_p characteristics of the used WTS

2.3 GRID model

The GSC, linked to the previously established MSC in a back-to-back configuration, both converters possess identical average models. GSC effectively regulates the DC bus voltage and establishes the reference reactive power at zero, thus ensuring the grid's quality by maintaining a unity power factor [24]. The d-q voltage components of the electrical network are stated as follows [25]:

$$\left.\begin{aligned} v_{df} &= R_f i_{dg} + \frac{L_{dg} di_{dg}}{dt} - L_f \omega_g i_{qg} + v_{dg} \\ v_{qf} &= R_f i_{qg} + \frac{L_{qg} di_{qg}}{dt} + L_f \omega_g i_{dg} + v_{qg} \end{aligned}\right\} \tag{10}$$

where, v_{dg}, v_{qg}, v_{df}, and v_{qf} are the *d* and *q*-axis voltages of the grid and converter side, respectively, and i_{dg} and i_{qg} are the *d* and *q*-axis filter currents. ω_g is the angular frequency of the grid voltage. R_f and L_f are the resistance and the inductance of the filter.

$$C\, v_{dc} \frac{dv_{dc}}{dt} = P_e - P_g \tag{11}$$

where, C is the dc-link capacitance, v_{dc} is the DC-link voltage, P_e and P_g are the quantification of power flowing to the dc-link and the power passing to the electrical grid respectively.

3. CONTROL SYSTEM

The proposed control system is depicted in Figure 3. The FS-MPC framework control both the MSC and GSC. PI controllers are designed to regulate the speed of the PMSM by integrating the speed control loop with the Maximum Power Point Tracking (MPPT) system and the GSC regulate the voltage of the DC link by the regulation of active and reactive power and ensures grid synchronization.

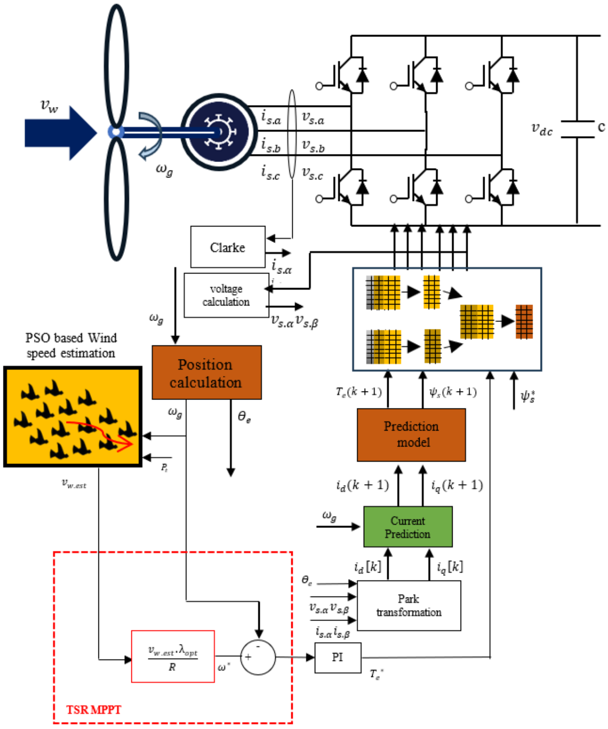

Figure 3. MSC proposed control system

3.1 Traditional FS-PTC scheme

FS-PTC operates by forecasting the torque and stator flux for a constrained array of potential switching states in a VSC. It identifies the optimal switching state (the one that most effectively minimizes torque and flux ripples) with a predetermined cost function. This cost function may encompass several objectives, variables, and constraints, each designated a specific weighting factor [26]. To develop the control technique, Eq. (6) can be substituted into Eq. (5) and resolved for :

$$\left.\begin{aligned} \frac{di_{ds}}{dt}(t) &= -\frac{R_s i_{ds}}{dt}(t) + \omega_e i_{qs}(t) + \frac{1}{L_d}v_{ds}(t) \\ \frac{di_{qs}}{dt}(t) &= -\frac{R_s i_{qs}}{dt}(t) - \omega_e i_{ds}(t) - \frac{\omega_e}{L_q}\psi_{pm} + \frac{1}{L_q}v_{qs}(t) \end{aligned}\right\} \tag{12}$$

The stator flux linkage magnitude and an angle can be calculated as follow:

$$|\psi_s| = \sqrt{\psi_{ds}^2 + \psi_{qs}^2} \tag{13}$$

$$\theta_s = tan^{-1}(\frac{\psi_{qs}}{\psi_{ds}}) \tag{14}$$

To implement the forward Euler technique on the continuous-time model in Eq. (12), it is essential to maintain the sampling time (T_s) is at or below one second. This facilitates the expression of the PMSG's discrete-time representation in the rotating dq-reference frame as follows:

$$\left.\begin{aligned} i_{ds}[k+1] &= \left(1 - \frac{T_s R_s}{L_d}\right) i_{ds}[k] \\ &+\omega_e T_s i_{qs}[k] + \frac{T_s}{L_d}u_{ds}[k] \\ i_{qs}[k+1] &= \left(1 - \frac{T_s R_s}{L_q}\right) i_{qs}[k] - \omega_e T_s i_{ds}[k] \\ &-\frac{\omega_e T_s}{L_q}\psi_{pm} + \frac{T_s}{L_q}u_{qs}[k] \end{aligned}\right\} \tag{15}$$

As a result, the stator flux and electro-magnetic torque are predicted in discrete time using the following expression:

$$\left.\begin{aligned} \psi_{ds}[k+1] &= L_d i_{ds}[k+1] + \psi_{pm} \\ \psi_{qs}[k+1] &= L_q i_{qs}[k+1] \end{aligned}\right\} \tag{16}$$

$$T_e[k+1] = \frac{3}{2}p\psi_{pm} i_{qs}[k+1] \tag{17}$$

The torque and stator flux have been designated as control variables. The stator voltage $u_{ds}[k]$ and $u_{qs}[k]$ can be mathematically expressed according to the arrangement of the switching state vector [27].

$$u_{dqs}[k] = T_p(\phi_r)^{-1} T_C u_s^{abc}[k] \tag{18}$$

$$T_p(\phi_r)^{-1} = \begin{bmatrix} cos(\phi_r) & sin(\phi_r) \\ -sin(\phi_r) & cos(\phi_r) \end{bmatrix} \tag{19}$$

$$T_C = \frac{2}{3}\begin{bmatrix} 1 & -\frac{1}{2} & -\frac{1}{2} \\ 0 & \frac{\sqrt{3}}{2} & -\frac{\sqrt{3}}{2} \end{bmatrix} \tag{20}$$

$$\begin{aligned} u_s^{abc}[k] &= \begin{bmatrix} u_{as} \\ u_{bs} \\ u_{cs} \end{bmatrix} \\ &= \frac{1}{3}v_{dc}[k] \begin{bmatrix} 2 & -1 & -1 \\ -1 & 2 & -1 \\ -1 & -1 & 3 \end{bmatrix} S^{abc}[k] \end{aligned} \tag{21}$$

where, $T_p(\phi_r)^{-1}$ denotes the inverse park matrice, T_C represents clarke transformation matrice, ϕ_r is the electrical rotor position in rad/s ($\phi_r = p\phi_m$), $u_s^{abc}[k]$ and v_{dc} refers to the three-phase voltage vector. Vector and DC-link voltage in volt respectively.

By assessing all potential combinations of the switching state vector $S^{abc}[k]$ eight distinct voltage vectors (VVs) can be generated, six active VVs and zero VVs. These VVs are employed to forecast seven successive values of the current $i_{ds}[k+1]$, subsequently followed by the prediction of the electromagnetic $T_e[k+1]$ and stator flux $\psi_s[k+1]$ [28]. The control algorithm functions in discrete time intervals, perpetually refining its predictions according to the latest observations and determining the ideal switching vector that minimizes the cost function specified in Eq. (23) [29].

$$\begin{aligned} g = |T_e{}^* - T_e[k+1]| + Ɱ \,\big||\psi_s{}^*| - |\psi_s[k+1]|\big| \\ + \mu \end{aligned} \tag{22}$$

with,

$$\left.\begin{aligned} &\mu = 0 && \text{if } T_e[k+1] \le T_e^{max} \\ &\mu = \infty && \text{if } T_e[k+1] > T_e^{max} \\ &\mu = 0 && \text{if } \sqrt{i_{ds}[k+1]^2 + i_{qs}[k+1]^2} \le i_s^{max} \\ &\mu = \infty && \text{if } \sqrt{i_{ds}[k+1]^2 + i_{qs}[k+1]^2} > i_s^{max} \end{aligned}\right] \tag{23}$$

$T_e{}^*$, $\psi_s{}^*$ and Ɱ are the reference torque reference statoric flux respectively and the weighting factor respectively. μ is a safety feature that limits the range of the torque and the starting current [30]. The reference torque comes from the speed control loop, where the speed is set to the reference speed in order to keep the TSR at its optimal value λ_{opt} as expresed in Eq. (24). This ensures the turbine captures as much wind energy as possible and converts it into mechanical energy effectively [31].

$$\lambda_{opt} = R\,\frac{\Omega_{t.opt}}{v} \tag{24}$$

3.2 PSO based wind speed estimation

The PSO method involves initialising a collection of particles with arbitrary positions and velocities within the specified search domain [32]. The objective function is derived from the discrepancy between the predicted and actual output power of the VSWT, as illustrated in Eq. (25). Each particle assesses the objective function and adjusts its positions and velocities based on its own best-known position and the best-known positions of neighbouring particles. This iterative process persists until convergence, at which stage the particles align with the optimal estimation of wind speed. The procedure is illustrated in Figure 4. The velocity is updated as follows [33, 34]:

$$\mathrm{v_i}(t+1) = \omega \mathrm{v_i}(t) + c_1 r\left(P_{best} - x_i(t)\right) + c_2 r\left(G_{best} - x_i(t)\right) \tag{25}$$

with,

$$x_i(t+1) = x_i(t) + v_i(t+1) \tag{26}$$

From Eq. (25) and Eq. (26) the particle position $x_i(t)$ (estimated wind speed) is updated according to the Equation:

$$x_i(t+1) = x_i(t) + \omega v_i(t) + c_1 r\left(P_{best} - x_i(t)\right) + c_2 r\left(G_{best} - x_i(t)\right) \tag{27}$$

$$F = \sum_{t=1}^{n} \left(P_{best}(t) - \widehat{P_i(t)}\right)^2 \tag{28}$$

where, c_1 and c_2 represents the social and cognitive parameters to adjust the balance between social influence and individual particle learning. ω signifies the inertia factor, $v_i(t)$ denotes the velocity vector, r represents random numbers uniformly distributed within the interval [0,1], P_{best}, G_{best}, N and $\widehat{P_i(t)}$ are the best individual position, the best social position, the total number of time steps and the power computed using the estimated wind speed, respectively.

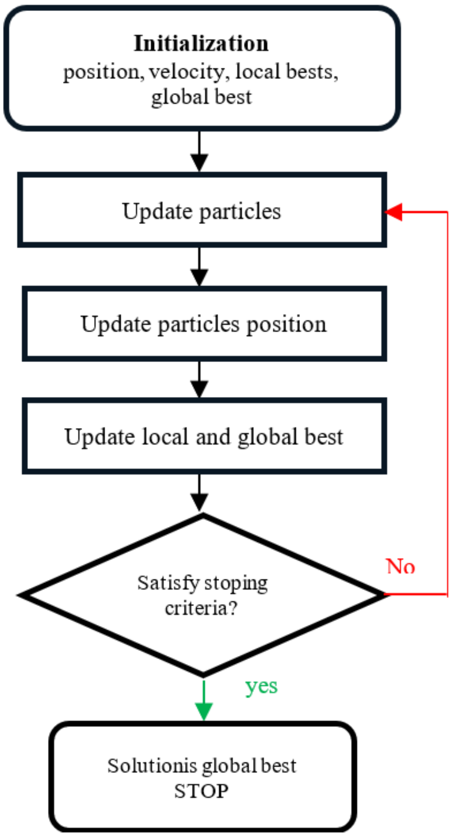

Figure 4. The flowchart of the PSO algorithm

Note: That the number of particles; affects computational cost and solution quality. And the inertia weight controls momentum, balancing exploration and exploitation (low inertia weight).

3.3 Weighting factors elimination

The main goal of the suggested method is to avoid using weighting factor by substituting it with a multi-objective ranking strategy. this approach predicated on the notion that the chosen voltage vector must facilitate an equitable minimisation of both objective functions. Unlike the conventional FS-PTC multi objective ranking-based FS-PTC, the fitness values of stator flux and torque are identical. The primary benefit of this proposed solution is the complete elimination of the tuning process for inner control-loop parameters, this technique is applied in the study [9] with induction motor. In the PTC multi objective ranking-based FS-PTC framework, the aggregate objective function is replaced with a multi-objective optimisation phase, facilitating equitable optimisation of the necessary control objectives. The method is founded on a strategy utilised for ranking populations in evaluative optimisation algorithms derived from genetic algorithms, although it is considerably simplified due to the small control set of feasible solutions [35].

The two distinct cost functions employed to tackle the problem of voltage vector selection in traditional PTC expressed as shown in Eq. (29): The values derived from each of them are organized in order. A ranking value is thereafter assigned to each mistake value. VVs $g_1 v_s$(k+1) and $g_2 v_s$(k+1) with higher error are getting a higher ranking and vice versa. The proposed ranking technique is illustrated in the sequence depicted in Figure 5.

$$\left.\begin{aligned} g_1 &= |T_e^* - T_e[k+1]| \\ g_2 &= \big||\psi_s^*| - |\psi_s[k+1]|\big| \end{aligned}\right\} \tag{29}$$

$$\left.\begin{aligned} g_1 v_s(k+1) &= r_1 v_s(k+1) \\ g_2 v_s(k+1) &= r_2 v_s(k+1) \end{aligned}\right\} \tag{30}$$

where, $r_i v_s$ are the ranking values related with g_i.

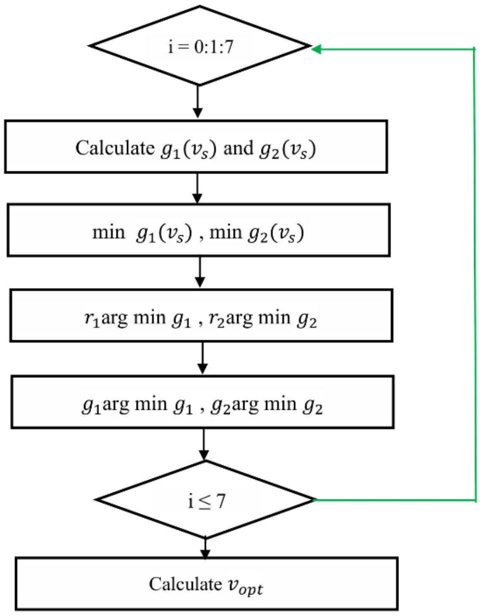

Figure 5. The steps of the ranking approach

3.3.1 Overall criteria

Now and by choosing the ranking with the minimal value, it can identify an optimal voltage vector from the point of view of one variable error. An average criterion is employed to determine this OVV among the possibilities, whereby the VV with the lowest average ranking is chosen, achieving a balanced compromise in tracking both torque and flow variables. The proposed optimization utilizing average ranking is presented as follows [36, 37] a ranking example is shown in Figure 6:

$$v_{opt} = \arg\min \frac{(r_1 v_s(\mathrm{k}+1))^2 + (r_2 v_s(\mathrm{k}+1))^2}{2} \tag{31}$$

Another way to implement the average ranking technique is by applying a distance metric, selecting the converter actuation whose ranking vector has the minimal Euclidean norm relative to the origin as shown in Eq. (32):

$$v_{opt} = \arg\min \sqrt{(r_1 v_s(\mathrm{k}+1))^2 + (r_2 v_s(\mathrm{k}+1))^2} \tag{32}$$

This represents the solution with the minimal deviation from the ideal point for both objectives.

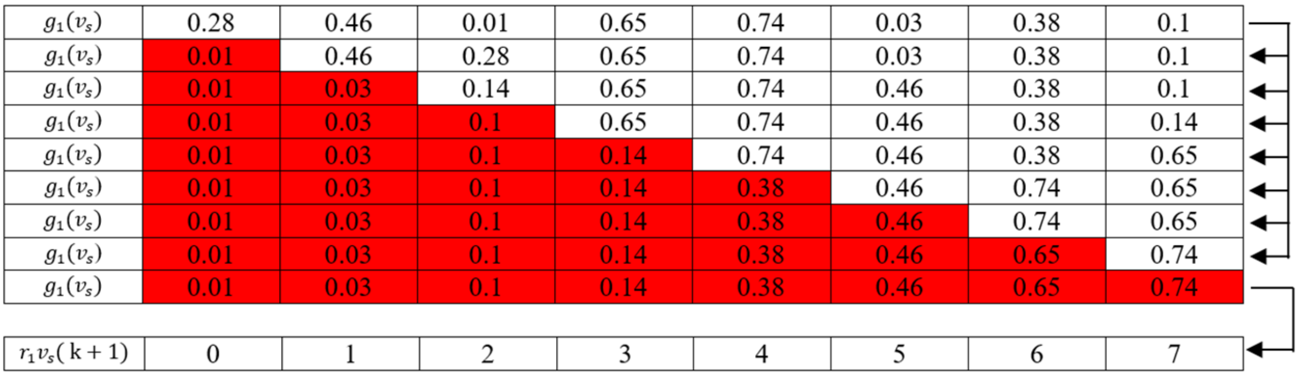

$g_1(v_s)$	0.28	0.46	0.01	0.65	0.74	0.03	0.38	0.1
$g_1(v_s)$	0.01	0.46	0.28	0.65	0.74	0.03	0.38	0.1
$g_1(v_s)$	0.01	0.03	0.14	0.65	0.74	0.46	0.38	0.1
$g_1(v_s)$	0.01	0.03	0.1	0.65	0.74	0.46	0.38	0.14
$g_1(v_s)$	0.01	0.03	0.1	0.14	0.74	0.46	0.38	0.65
$g_1(v_s)$	0.01	0.03	0.1	0.14	0.38	0.46	0.74	0.65
$g_1(v_s)$	0.01	0.03	0.1	0.14	0.38	0.46	0.74	0.65
$g_1(v_s)$	0.01	0.03	0.1	0.14	0.38	0.46	0.65	0.74
$g_1(v_s)$	0.01	0.03	0.1	0.14	0.38	0.46	0.65	0.74

$r_1 v_s(\mathrm{k}+1)$	0	1	2	3	4	5	6	7

Figure 6. Ranking approach steps application example

3.3.2 Sorting algorithm

This section describes the process of ordering potential solutions based on their assigned rankings. The implementation employs a recursive quicksort approach [38]. As a classic divide-and-conquer method, quicksort operates by initially partitioning the input list into two separate groups: elements with lower values and those with higher values. The algorithm then proceeds to sort these subgroups through recursive application of the same process. The quicksort procedure executes through these sequential operations [39]:

1. **Pivot Selection**: Choose a pivot element from the array.
2. **Array Partitioning**:
    - Rearrange elements such that all items smaller than the pivot precede it.
    - Position all elements larger than the pivot after it.
    - This operation places the pivot in its correct sorted position.
3. **Recursive Processing**:
    - Apply the algorithm recursively to the portion containing elements less than the pivot.
    - Similarly, recursively process the portion with elements greater than the pivot.

3.4 Tip speed ratio MPPT

Wind energy systems exhibit complex nonlinear dynamics in their power-speed (P–Ω) characteristics, where maximum power extraction is only achievable at a single optimal operating point determined by instantaneous wind conditions. This fundamental constraint necessitates sophisticated control strategies to maintain operation at the maximum power point (MPP) across varying wind speeds [40].

Various MPPT strategies are employed to optimise the power output and ensure it remains at its greatest value throughout different wind speed conditions such as hill climb search, power signal feedback, the incremental conductance method,optimal torque (OT) [41] and the TSR technique. The TSR MPPT technique aims to regulate the tip speed of the rotor blades in proportion to the wind speed and can be computed as follows [42, 43]:

$$\lambda_{opt} = R\frac{\Omega_{t.opt}}{v} \tag{33}$$

This ideal TSR guarantees the utmost aerodynamic efficiency, resulting in the highest possible power production and the exctracted power.

$$P_{m.max} = \frac{1}{2} C_{pmax}(\lambda_{opt}, \beta).\rho.\pi.R^2.v_w{}^3 \tag{34}$$

4. RESULTS

4.1 Simulation results

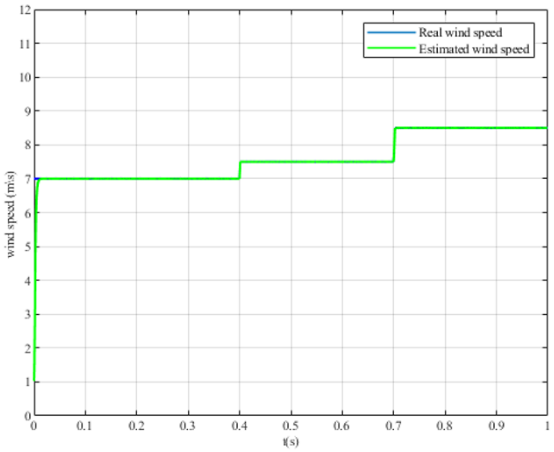

Figure 7. Wind speed estimation

In this section, simulation results are analyzed to assess the performance of proposed FS-PTC technique during variable wind speeds. As depicted in Figure 7 PSO based estimation shows well tracking of the measured wind speed. All simulations were conducted using MATLAB/SIMULINK. An 3kW WECS simpower model was used for this evaluation. Figure 8 illustrates the turbine's mechanical power output, following the same curve as the wind speed profile. Figure 9 shows the mechanical speed response of the system, comparing the reference speed that calculated using the TSR MPPT Eq. (33) with the measured speed, this figure shows that the PMSG speed closely tracks its reference value. This close tracking shows that the system is well-controlled and remains stable, smoothly adjusting to changes in the reference speed. Figure 10 demonstrates that the C_p is maintained at its optimal value. Figure 11 shows the stator flux trajectory, which is represented as a circular path. The diameter of the circle is 0.43 with the proposed approach noticeably reducing any fluctuations in the flux trajectory.

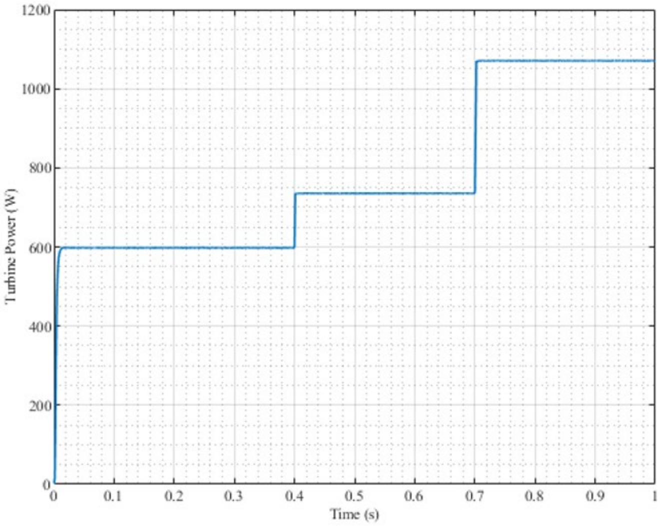

Figure 8. Turbine mechanical power

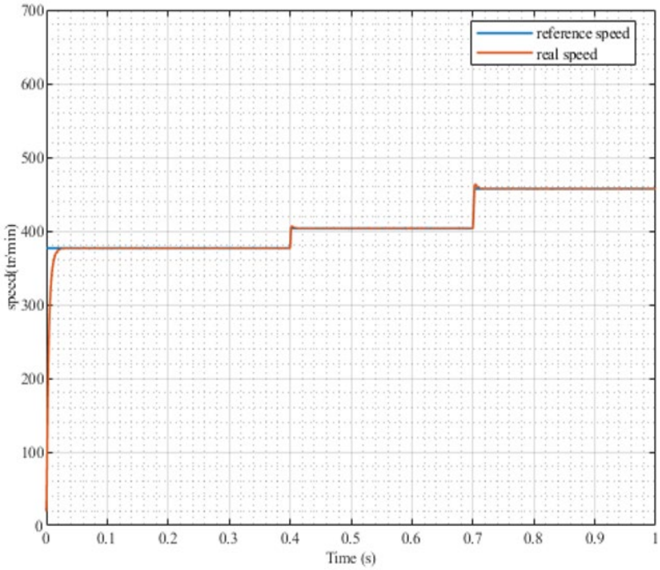

Figure 9. PMSG speed

Figure 12 demonstrates that the PMSG torque closely follows its reference torque throughout the entire observation period. This indicates that the PMSG is operating efficiently and its control system is effectively regulating the generator's torque output to align with the desired reference value. Additionally, the DC link voltage was observed to closely follow the reference as Figure 13 this is is essential for ensuring the overall performance and stability of the power conversion system. Figure 14 shows the GSC three phases generated currents exhibit a sinusoidal waveform with a steady frequency, while its amplitude varies depending on wind speed profile. As we can see in Figure 15 the injected power closely matches the reference power, demonstrating accurate tracking. This strong alignment between the two indicates that the control system is working effectively, ensuring that the power delivered to the grid stays on target. Figure 16 the injected reactive power remains consistently at zero that indicating effective control to maintain a purely active power injection.

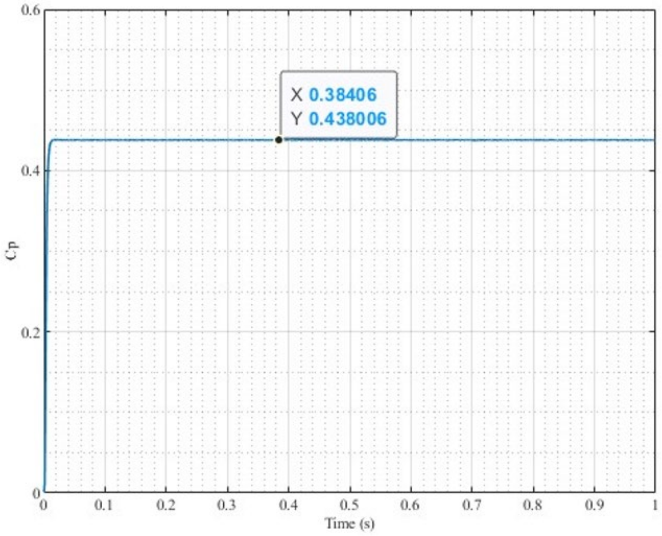

Figure 10. TSR and C_p curve

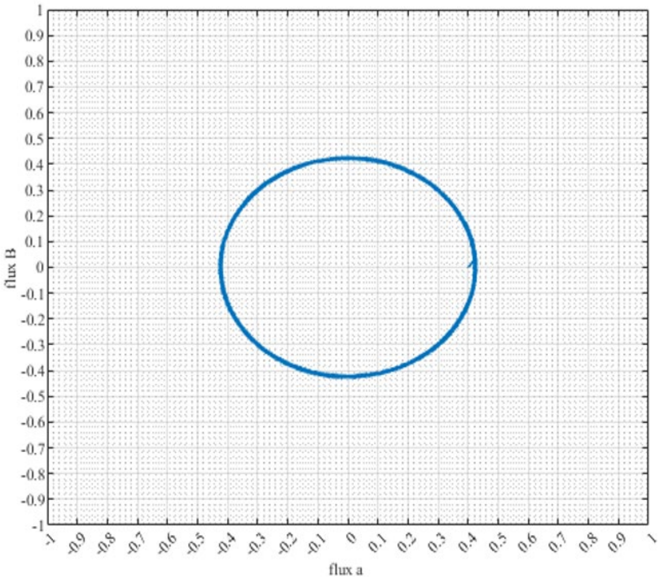

Figure 11. Flux trajectory in α-β farm

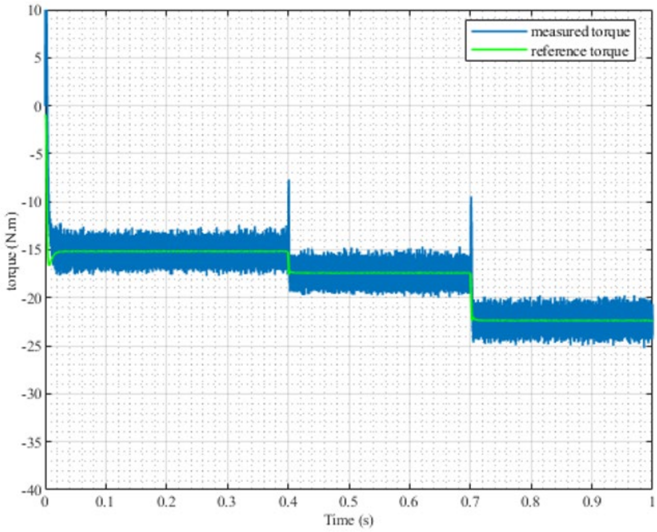

Figure 12. PMSG torque

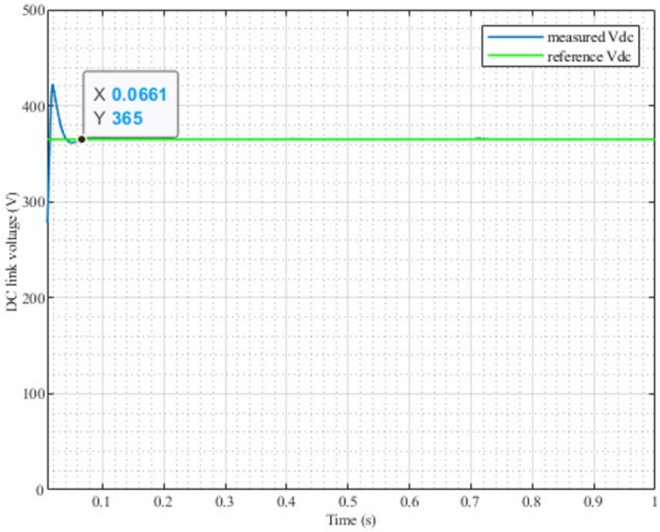

Figure 13. DC link voltage

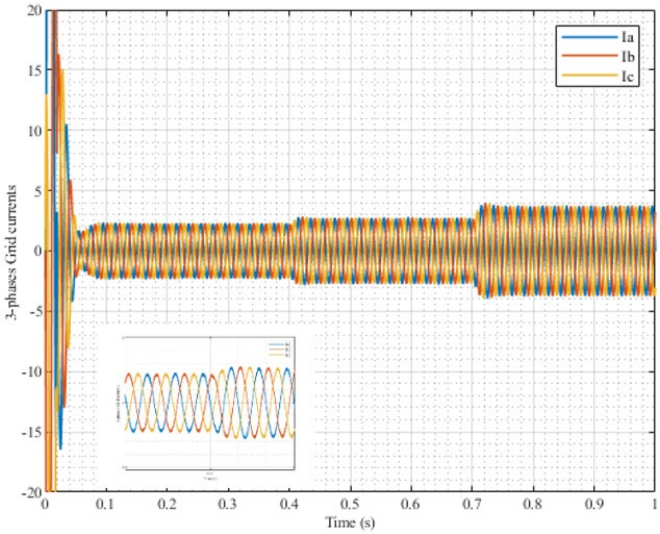

Figure 14. GSC currents

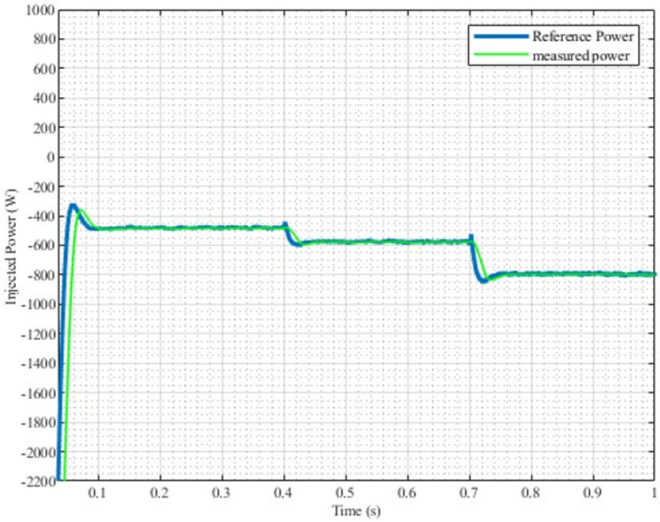

Figure 15. Active injected power

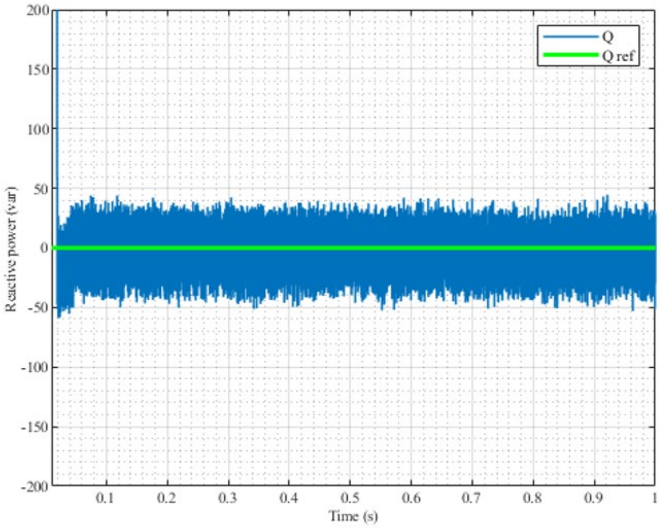

Figure 16. Injected reactive power

4.2 Exprimantal results

Following multiple stages of development, the wind power conversion system was tested experimentally using a setup in the LGEB laboratory, illustrated in Figure 17. The system was managed by two PCs equipped with MATLAB-Simulink, connected through a real-time interface (RTI). The testing setup included a 4 kW PMSG (the electrical and mechanical parameters of the PMSG are listed in Table 1) directly powered by a wind emulator that utilized a 3 kW three-phase asynchronous motor.

To estimate wind speed, the turbine power and PMSG speed are sent from the DAC output of the dSPACE DS1104 (No. 1) to the ADC inputs of the DSP LAUNCHXL-F28379D card. The system uses two Semikron power converters arranged in a back-to-back configuration, linked by a 2200 µF capacitor, to interface the PMSG rotor with the electrical grid. Both converters are managed by a single dSPACE DS1104 (No. 2) controller.

Figure 17. VSWT test bench

1. Autotransformer
2. Multimeter
3. Fluke 435 series ii
4. Host 1 PC
5. PC for data acquisition
6. PMSG
7. Induction motor (emulator)
8. MSC
9. Adaptation card 2
10. 15 volt power supply
11. GSC
12. L Filter
13. Dspace1104
14. MSC-GSC separation switch

The experimental results presented in Figure 18 demonstrate the effectiveness of the proposed PSO-based wind speed observer under variable wind speed profile. As shown in the figure, the estimated wind speed closely tracks the actual measured values. The system's response to step changes in wind speed shows minimal overshoot (consistently below 5% of the steady-state value) while maintaining precise tracking during gradual variations.

Table 1. Parameters of PMSG

Parameter	Value	Parameter	Value
Nominal power	4 Kw	Stator flow	0.44 Wb
Stator Resistance	0.8 Ω	Rated torque	19.5 Nm
Nom frequency	200 Hz	Number of pole pairs	4
Stator Inductance	0.128 H	moment of inertia	0.03Kgm²
Rotor Inductance	0.128 H	Rated speed	3000 rpm
Rated current	8 A		

Figure 19 showed that the measured rotor speed showing precise tracking of the reference command across various operating conditions. During steady-state operation, the system achieves near-perfect speed matching with 99.2% accuracy and maintains maximum speed deviations within just ±0.15% of the rated value.

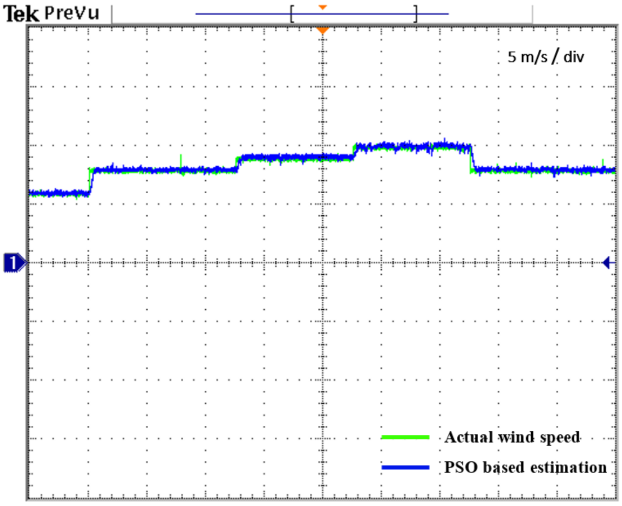

Figure 18. Actual and estimated wind speed with PSO

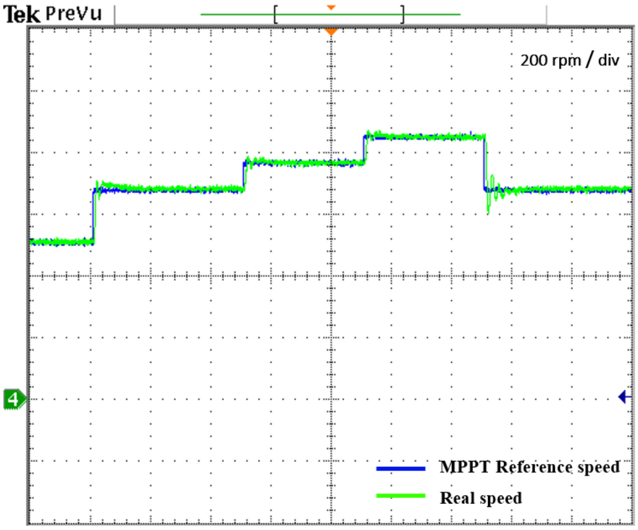

Figure 19. PMSG mechanical speed response

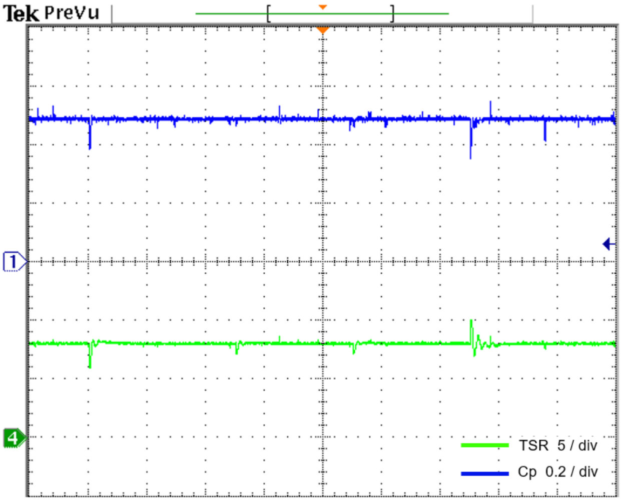

Figure 20. TSR and Cp curve during actual wind profile

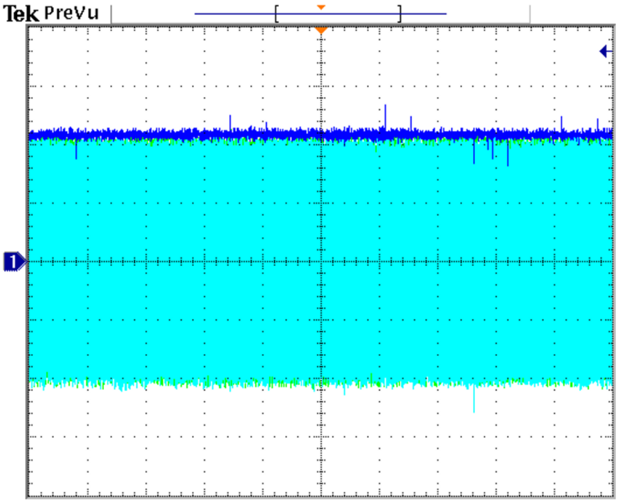

Figure 21. Flux a flux b flux

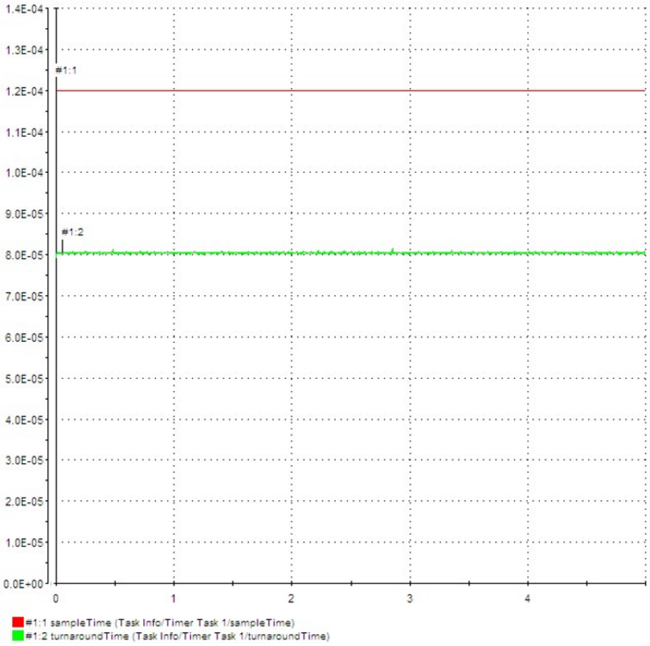

Figure 22. Computational timing characteristics

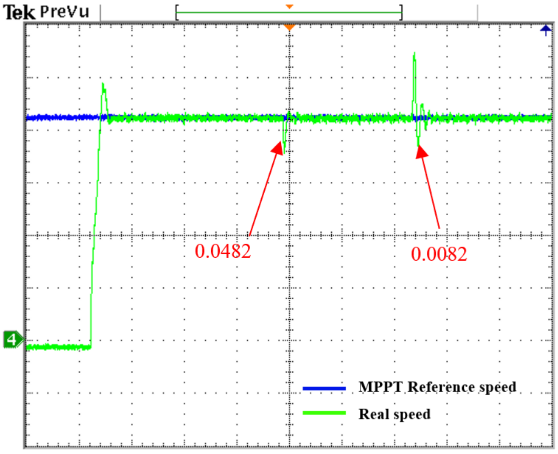

Figure 23. System s robustness under inductance variation

The experimental analysis demonstrates the effectiveness of the TSR MPPT algorithm in optimizing wind energy conversion. As evidenced in Figure 20, the control system successfully maintains operation at peak efficiency, consistently regulating the power coefficient C_p at approximately 0.48 while simultaneously tracking the optimal tip-speed ratio $\lambda_{opt.}$ This high-performance operation is achieved through precise steady-state control maintaining Cp within ±0.01 of its maximal value. Figure 21 demonstrates the stationary frame (αβ) flux components, showing ideal sinusoidal waveforms that precisely track the nominal flux which is is critical for high-efficiency operation.

Figure 22 examines the real-time computational characteristics of the FS-PTC algorithm, focusing on two key timing parameters that critically impact system performance the value of the turnaround time demonstrating sufficient margin for implementation on standard digital signal processors. These timing characteristics directly translate to superior drive performance. The short turnaround time enables deadbeat-like torque response with delays contained within one sample period, crucial for accurate tracking of MPPT speed references.

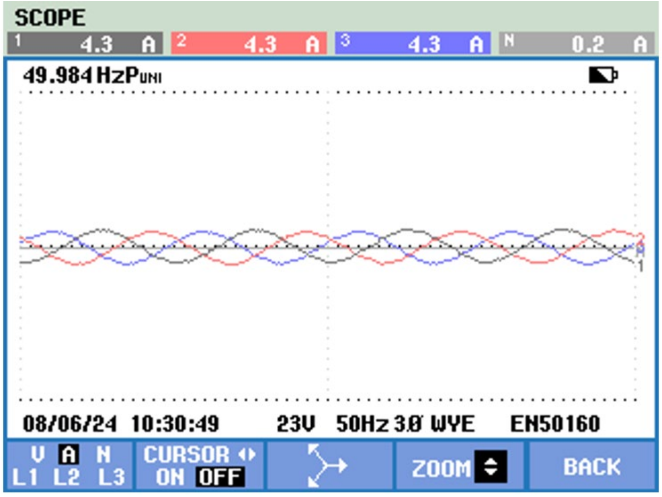

Figure 24. 3-Phases currents GSC

Figure 23 demonstrates the exceptional robustness of the FS-PTC in maintaining precise speed tracking of the MPPT reference, despite variations in the machine parameters (L_d and L_q). Higher Inductance increases the machine's inductive inertia that cause a speed undershoot

A reduction in L_d/L_q decreases the electrical time constant, leading to temporary overshoot in speed tracking.

The three-phase currents of the GSC exhibit highly sinusoidal waveforms with THD value equal to 3.1%, as illustrated in the Figures 24 and 25 respectively, demonstrating effective power regulation and synchronization with the grid voltage. Figure 26 and Figure 27 demonstrating stable and well-regulated performance and low THD value which meets IEEE 1547-2018 and IEC 61000-3-12 standards this clean sinusoidal shape with no visible distortion or clipping, and balanced voltage as shown in Figure 28 indicating proper PWM control.

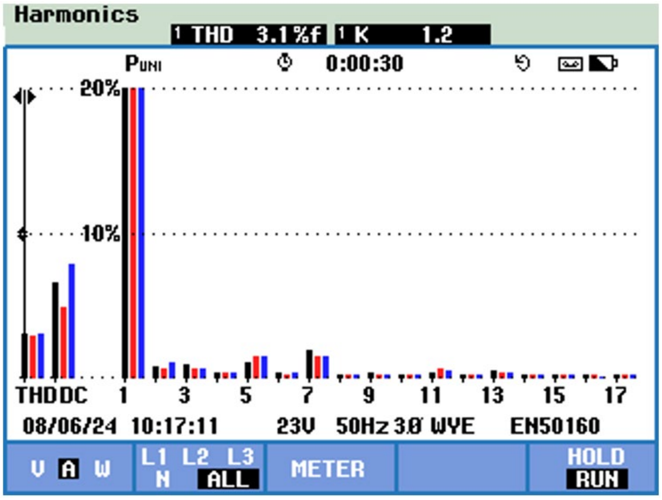

Figure 25. Currents THD

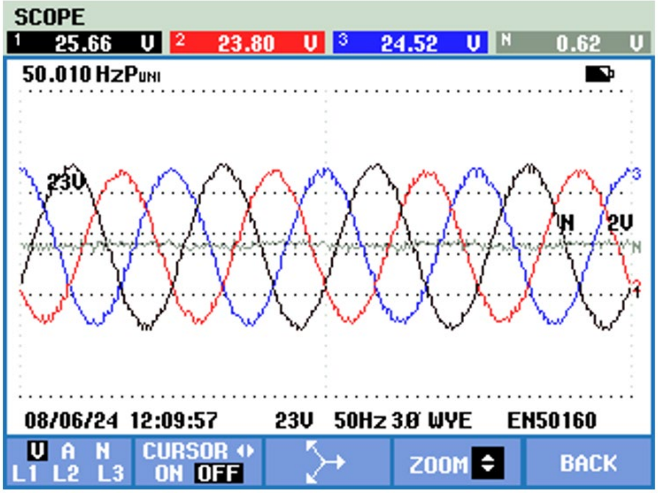

Figure 26. 3-Phases voltage GSC

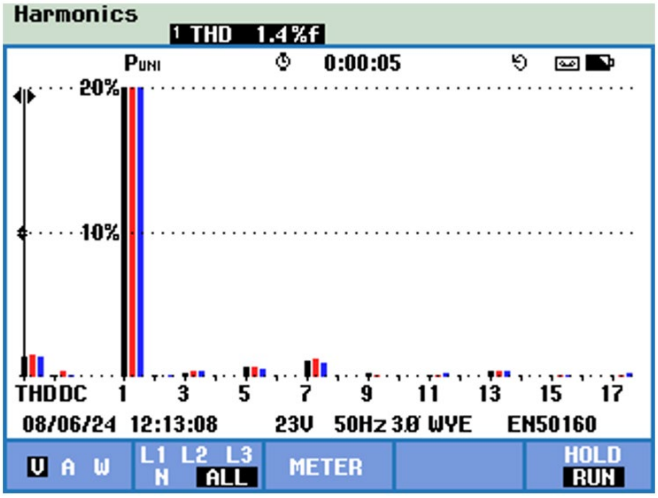

Figure 27. Voltage THD

The power flow of the grid-side converter system are presented in Figure 29, showing the measured active power (kW), apparent power (kVA), reactive power (kVAR), and power factor (PF). The negative active power value clearly indicates successful power injection from the GSC to the utility grid, confirming proper system operation in generation mode. A small positive reactive power value of 0.06 kVAR demonstrates the system's capability to provide reactive power support, primarily enabled by the autotransformer configuration. The power factor of -0.99 provides important operational insights: the negative sign verifies the PMSG is functioning as a power source to the grid, while the near-unity magnitude reflects exceptionally efficient power transfer with minimal energy losses. This optimal power factor value indicates precise synchronization between the converter and grid and maximized active power delivery efficiency.

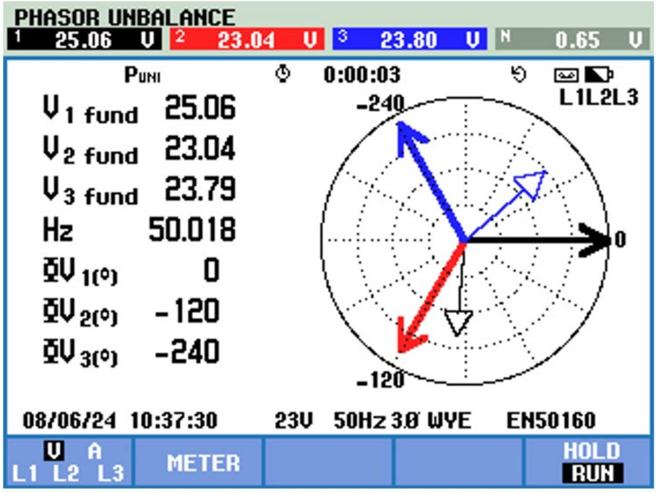

PHASOR UNBALANCE

1 25.06 V | 2 23.04 V | 3 23.80 V | N 0.65 V

V1 fund 25.06
V2 fund 23.04
V3 fund 23.79
Hz 50.018
ΦV 1(°) 0
ΦV 2(°) -120
ΦV 3(°) -240

08/06/24 10:37:30 23V 50Hz 3Ø WYE EN50160

Figure 28. Voltage phasor unbalance GSC

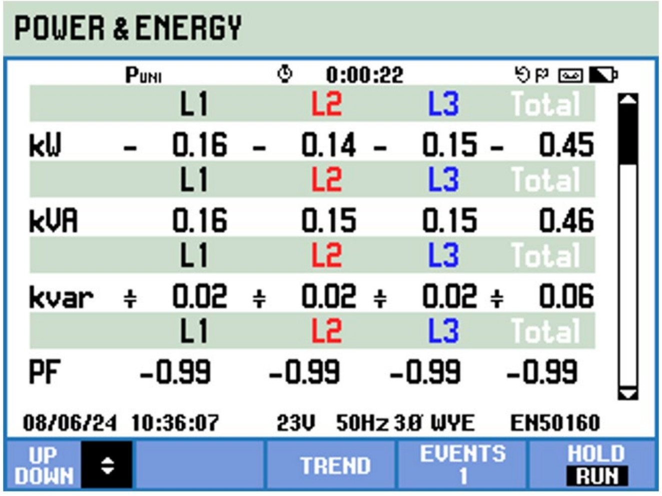

POWER & ENERGY

	L1	L2	L3	Total
kW	- 0.16	- 0.14	- 0.15	- 0.45
kVA	0.16	0.15	0.15	0.46
kvar	÷ 0.02	÷ 0.02	÷ 0.02	÷ 0.06
PF	-0.99	-0.99	-0.99	-0.99

08/06/24 10:36:07 23V 50Hz 3Ø WYE EN50160

Figure 29. Power and energy measurement

5. CONCLUSION

This study has introduced an innovative sensorless wind speed estimation technique for grid-connected wind turbines, integrating PSO with Multi-Objective PTC. The proposed approach successfully addresses the limitations of traditional wind speed measurement methods by eliminating the need for physical anemometers, thereby reducing system costs and complexity while maintaining high estimation accuracy. A key innovation of this work is the development of a multi-objective ranking system that eliminates the need for weighting factors in the control optimization process. This approach enables automatic prioritization of competing control objectives - including torque ripple minimization, flux regulation.

The multi-objective FS-PTC strategy, enhanced by this ranking method, effectively optimized multiple performance indices simultaneously while maintaining computational efficiency suitable for real-time implementation. Comprehensive simulation and experimental validation under various operating conditions confirmed the method's effectiveness.

This work provides both theoretical insights and practical solutions for the wind power industry, establishing a foundation for future developments in intelligent, self-optimizing control systems for wind energy applications.

ACKNOWLEDGEMENTS

Sincere gratitude to the LGEB for the invaluable support during this research, equipment in the laboratory was crucial for experimental validation.

REFERENCES

[1] Kuncoro, I.W., Arifin, Z., Budiana, E.P., Hijriawan, M. (2023). Improvement performance twisted savonius wind turbine on hybrid system: Effect of flat plate deflector installation. International Journal of Heat and Technology, 41(3): 742-748. https://doi.org/10.18280/ijht.410330

[2] Al-Hadidi, A., Duwairi, H. (2019). Wind turbine performance under fluctuating pressure gradient of laminar and turbulent air flows. European Journal of Electrical Engineering, 21(5): 447-456. https://doi.org/10.18280/ejee.210507

[3] Hallouz, M., Kabeche, N., Moulahoum, S., Kechidi, Z. (2023). Experimental investigation of DFIG-based wind energy conversion system using fuzzy logic control. Periodica Polytechnica Electrical Engineering and Computer Science, 67(3): 260-267. https://doi.org/10.3311/PPee.21233

[4] Tola, O.J., Umoh, E.A., Yahaya, E.A., Olusegun, O.E. (2022). Permanent magnet synchronous generator connected to a grid via a high speed sliding mode control. International Journal of Robotics and Control Systems, 2(2): 379-395. https://doi.org/10.31763/ijrcs.v2i2.701

[5] Boureguig, K., Ouagueni, F., Soued, S. (2024). Dynamic performance enhancement of DFIGURE wind turbine using an active disturbance rejection control-based sliding mode control. Studies in Engineering and Exact Sciences, 5(2): e9472-e9472. https://doi.org/10.54021/seesv5n2-361

[6] Luján, J.C.G., Monteagudo, F.E.L., y Ramos, J.D.L.T., Rodríguez, L.D.C.R. (2024). Characterization of a low power wind turbine prototype for interconnection to the grid. Itegam-Jetia, 10(46): 22-26. https://doi.org/10.5935/jetia.v10i46.1110

[7] Mahmoud, M.M., Aly, M.M., Abdel-Rahim, A.M.M. (2020). Enhancing the dynamic performance of a wind-driven PMSG implementing different optimization techniques. SN Applied Sciences, 2: 1-19. https://doi.org/10.1007/s42452-020-2439-3

[8] Echeikh, H., Trabelsi, R., Kesraoui, H., Iqbal, A., Mimouni, M.F. (2020). Torque ripples improvement of direct torque controlled five-phase induction motor drive using backstepping control. International Journal of Power Electronics and Drive Systems, 11(1): 64-74. https://doi.org/10.11591/ijpeds.v11.i1.pp64-74

[9] Chebaani, M., Ebeed, M., Abdellatif, W.S., Elbarbary, Z.S., Nouraldin, N.A. (2023). Design and implementation of an improved finite-state predictive direct torque control for induction motor with new weighting factor elimination. IEEE Access, 11: 58169-58187. https://doi.org/10.1109/ACCESS.2023.3283983

[10] Chirantan, S., Pati, B.B. (2024). Dynamics assessment of an inverter fed induction motor drive by an improved predictive controller leveraging finite control set mechanism. Itegam-Jetia, 10(47): 83-94. https://doi.org/10.5935/jetia.v10i47.1098

[11] Zheng, J., Zhao, W., Ji, J., Zhu, J., Lee, C.H. (2020). Sleeve design of permanent-magnet machine for low rotor losses. Chinese Journal of Electrical Engineering, 6(4): 86-96. https://doi.org/10.23919/CJEE.2020.000033

[12] Prince, M.K.K., Arif, M.T., Haque, M.E., Gargoom, A., Oo, A.M.T. (2023). Design and implementation of finite control set MPC with an LCL filter for grid-tied PMSG based wind turbine. International Journal of Electrical Power & Energy Systems, 152: 109197. https://doi.org/10.1016/j.ijepes.2023.109197

[13] Aberkane, H., Sakri, D., Rahem, D. (2021). Enhanced finite-state predictive torque control of induction motor using space vector modulation. Przegląd Elektrotechniczny, 97(4): 41-47. https://doi.org/10.15199/48.2021.04.07

[14] Zhang, Y., Zhang, Z., Babayomi, O., Li, Z. (2023). Weighting factor design techniques for predictive control of power electronics and motor drives. Symmetry, 15(6): 1219. https://doi.org/10.3390/sym15061219

[15] Zhang, X., Yan, K., Cheng, M. (2021). Two-stage series model predictive torque control for PMSM drives. IEEE Transactions on Power Electronics, 36(11): 12910-12918. https://doi.org/10.1109/TPEL.2021.3075711

[16] Rojas, C.A., Kouro, S., Perez, M., Villarroel, F. (2015). Multiobjective fuzzy predictive torque control of an induction machine fed by a 3L-NPC inverter. In 2015 IEEE International Symposium on Predictive Control of Electrical Drives and Power Electronics (PRECEDE), Valparaiso, Chile, pp. 21-26. https://doi.org/10.1109/PRECEDE.2015.7395507

[17] Muddineni, V.P., Bonala, A.K., Sandepudi, S.R. (2016). Enhanced weighting factor selection for predictive torque control of induction motor drive based on VIKOR method. IET Electric Power Applications, 10(9): 877-888. https://doi.org/10.1049/iet-epa.2016.0057

[18] Muddineni, V.P., Sandepudi, S.R., Bonala, A.K. (2017). Finite control set predictive torque control for induction motor drive with simplified weighting factor selection using TOPSIS method. IET Electric Power Applications, 11(5): 749-760. https://doi.org/10.1049/iet-epa.2016.0503

[19] Jena, D., Rajendran, S. (2015). A review of estimation of effective wind speed based control of wind turbines. Renewable and Sustainable Energy Reviews, 43: 1046-1062. https://doi.org/10.1016/j.rser.2014.11.088

[20] Yuhendri, M., Muskhir, M., Taali, T. (2019). A novel optimum tip speed ratio control of low speed wind turbine generator based on type-2 fuzzy system. Bulletin of Electrical Engineering and Informatics, 8(4): 1189-1197. https://doi.org/10.11591/eei.v8i4.1450

[21] Kouadria, M.A., Kouadria, S., Chaib, H. (2024). Sliding mode control for doubly fed induction generators system-based a wind turbine. Studies in Engineering and Exact Sciences, 5(2): e7199-e7199. https://doi.org/10.54021/seesv5n2-139

[22] Al-Khayyat, A.S., Abed, A.K., Ridha, A.A. (2023). Measured and estimated wind speed of a stand-alone energy system with controlled bi-directional DC-DC battery bank. Bulletin of Electrical Engineering and Informatics, 12(5): 2651-2664. https://doi.org/10.11591/eei.v12i5.4809

[23] Salih, B.M., Hamoodi, S.A., Hamoodi, A.N. (2024). Enhancing the behavior of small scale wind turbine based on fuzzy logic system. Journal Européen des Systèmes Automatisés, 57(1): 147-153. https://doi.org/10.18280/jesa.570115

[24] Tabbakh, M., Rouabhi, R., Herizi, A., Djeriou, S., Zemmit, A. (2024). Robust control based on type-2 fuzzy logic for permanent magnet synchronous motor (PMSM). Studies in Engineering and Exact Sciences, 5(2): e8086-e8086. https://doi.org/10.54021/seesv5n2-239

[25] Boudali, A., Negadi, K., Bouradi, S., Berkani, A., Marignetti, F. (2021). Design of nonlinear backstepping control strategy of PMSG for hydropower plant power generation. Journal Européen des Systèmes Automatisés, 54(1): 1-8. https://doi.org/10.18280/jesa.540101

[26] Habibullah, M., Lu, D.D.C., Xiao, D., Rahman, M.F. (2015). A computationally efficient FS-PTC for IM with minimum voltage vectors. In 2015 IEEE 11th International Conference on Power Electronics and Drive Systems, Sydney, NSW, Australia, pp. 992-997. https://doi.org/10.1109/PEDS.2015.7203420

[27] Shehata, E.G. (2017). A comparative study of current control schemes for a direct-driven PMSG wind energy generation system. Electric Power Systems Research, 143: 197-205. https://doi.org/10.1016/j.epsr.2016.10.039

[28] Chebaani, M., Goléa, A., Benchouia, M.T., Goléa, N. (2017). Sliding mode predictive control of induction motor fed by five-leg AC–DC–AC converter with DC-link voltages offset compensation. Journal of Control, Automation and Electrical Systems, 28: 597-611. https://doi.org/10.1007/s40313-017-0334-y

[29] Zhang, Z., Cui, Z., Zhang, Z., Kennel, R., Rodríguez, J. (2019). Advanced control strategies for back-to-back power converter PMSG wind turbine systems. In 2019 IEEE International Symposium on Predictive Control of Electrical Drives and Power Electronics (PRECEDE), Quanzhou, China, pp. 1-6. https://doi.org/10.1109/PRECEDE.2019.8753366

[30] Das, P., Abdelrahem, M., Farhan, A., Ismeil, M.A., Kennel, R. (2019). Predictive direct torque control of permanent magnet synchronous generators (PMSGs) without weighting factors. In 2019 IEEE Conference on Power Electronics and Renewable Energy (CPERE), Aswan, Egypt, pp. 296-301. https://doi.org/10.1109/CPERE45374.2019.8980112

[31] Aissaoui, A., Khouidmi, H., Benzouaoui, A., Bessedik, B. (2021). Nonlinear predictive control method for maximizing wind energy extraction of variable speed wind turbines under turbulence. Journal Européen des Systèmes Automatisés, 54(5): 661-670. https://doi.org/10.18280/JESA.540501

[32] Ghilani, A., Terki, A., Alili, Z., Ghodbane, A.M., Belaroussi, O. (2024). Experimental validation of PSO and GWO-based MPPT for a single-stage three-phase grid-connected PV system under partial shading. Journal Européen des Systèmes Automatisés, 57(5): 1387-1395. https://doi.org/10.18280/jesa.570514

[33] Abo-Khalil, A.G., Eltamaly, A.M., RP, P., Alghamdi, A.S., Tlili, I. (2020). A sensorless wind speed and rotor position control of PMSG in wind power generation systems. Sustainability, 12(20): 8481. https://doi.org/10.3390/su12208481

[34] Eltamaly, A.M., Al-Saud, M.S., Abokhalil, A.G., Farh, H.M. (2020). Photovoltaic maximum power point tracking under dynamic partial shading changes by novel adaptive particle swarm optimization strategy. Transactions of the Institute of Measurement and Control, 42(1): 104-115. https://doi.org/10.1177/0142331219865627

[35] Gambier, A. (2008). MPC and PID control based on multi-objective optimization. In 2008 American Control Conference, Seattle, WA, USA, pp. 4727-4732. https://doi.org/10.1109/ACC.2008.4587241

[36] Bentley, P.J., Wakefield, J.P. (1998). Finding acceptable solutions in the pareto-optimal range using multiobjective genetic algorithms. In Soft Computing in Engineering Design and Manufacturing, London, pp. 231-240. https://doi.org/10.1007/978-1-4471-0427-8_25

[37] Rojas, C.A., Rodriguez, J., Villarroel, F., Espinoza, J.R., Silva, C.A., Trincado, M. (2012). Predictive torque and flux control without weighting factors. IEEE Transactions on Industrial Electronics, 60(2): 681-690. https://doi.org/10.1109/TIE.2012.2206344

[38] Villarroel, F., Espinoza, J.R., Rojas, C.A., Rodriguez, J., Rivera, M., Sbarbaro, D. (2012). Multiobjective switching state selector for finite-states model predictive control based on fuzzy decision making in a matrix converter. IEEE Transactions on Industrial Electronics, 60(2): 589-599. https://doi.org/10.1109/TIE.2012.2206343

[39] Kernighan, B.W., Ritchie, D.M. (1988). The C programming language. Prentice-Hall.

[40] Azzouz, S., Messalti, S., Harrag, A. (2019). A novel hybrid MPPT controller using (P&O)-neural networks for variable speed wind turbine based on DFIG. Modelling, Measurement and Control A, 92(1): 23-29. https://doi.org/10.18280/mmc_a.920104

[41] Govinda, C.V., Udhay, S.V., Rani, C., Wang, Y., Busawon, K. (2018). A review on various MPPT techniques for wind energy conversion system. In 2018 International conference on computation of power, energy, Information and Communication (ICCPEIC), Chennai, India, pp. 310-326. https://doi.org/10.1109/ICCPEIC.2018.8525219

[42] Belaid, S., Rekioua, D., Oubelaid, A., Ziane, D., Rekioua, T. (2022). Proposed hybrid power optimization for wind turbine/battery system. Periodica Polytechnica Electrical Engineering and Computer Science, 66(1): 60-71. https://doi.org/10.3311/PPEE.18758

[43] Nasiri, M., Milimonfared, J., Fathi, S.H. (2014). Modeling, analysis and comparison of TSR and OTC methods for MPPT and power smoothing in permanent magnet synchronous generator-based wind turbines. Energy Conversion and Management, 86: 892-900. https://doi.org/10.1016/j.enconman.2014.06.055

NOMENCLATURE

VSWT	Variabl speed wind turbin
TSR	Tip speed ratio maximum power point
MPPT	Tracking
AVVs	Actives voltage vectors
ZVVs	Zero voltage vectors
PMSG	Permanent Magnet Synchronous Generator
WECSs	Wind energy conversion systems
FOC	Field-Oriented Control
DTC	Direct torque control
FSPTC	Finite state predictive torque control
MPC	Model predictive control
PTC	Predictive torque control
PPC	Predictive power control
FS	Finite state
VSC	Voltage source conveter
HAWT	Horizontal-axis wind turbine